



Chemical segregation and precipitation at anti-phase boundaries in thermoelectric Heusler-Fe₂VAl

Leonie Gomell^a, Shyam Katnagallu^{a,1}, Abou Diack Rassellio^b, Stefan Maier^c, Loïc Perrière^b, Christina Scheu^a, Eric Alleno^b, Baptiste Gault^{a,d,*}

^a Max-Planck-Institut für Eisenforschung, Max-Planck-Str. 1, 40237, Düsseldorf, Germany

^b Univ Paris Est Creteil, CNRS, ICMPE (UMR7182), 2 rue Henri Dunant, F-94320, Thiais, FRANCE

^c Institute of Physics IA, RWTH Aachen University, 52074 Aachen, Germany

^d Department of Materials, Royal School of Mines, Imperial College London, London, UK

ARTICLE INFO

Article history:

Received 28 March 2020

Revised 22 April 2020

Accepted 25 April 2020

Keywords:

Thermoelectric materials

Melt spinning

Atom probe tomography

Field-ion-microscopy

Microstructure

ABSTRACT

Fe₂VAl exhibits promising properties for thermoelectric applications. Here, we investigated the microstructure of melt spun Fe₂VAl using electron microscopy, atom probe tomography and field ion microscopy. We observe platelet-shaped VC_xN_y precipitates in the vicinity of antiphase boundaries (APB) oriented along the {100}-plane. The mean distance between these precipitates is (140 ± 40) nm. This distance is shorter than the mean free phonon path at room temperature in Fe₂VAl. Thus, these VC_xN_y precipitates, combined with the APB may efficiently lower the thermal conductivity of the alloy.

© 2020 Acta Materialia Inc. Published by Elsevier Ltd. All rights reserved.

The necessity for generating low-carbon energy has led to extensive research in the field of thermoelectric (TE) materials in recent years. TE devices can directly transform waste heat into usable energy, are silent, scalable, and barely require any maintenance [1]. However, TE generators are still primarily used in niche applications, e.g. remote power supplies, such as in deep-space missions [2], where reliability outweighs performance. Other possible applications such as automotive TE generators or solar thermal power generation are conceivable, but technological hurdles need to be overcome [3]. State-of-the-art TE materials such as Skutterudites [4], Bi₂Te₃ [5], Sb₂Te₃ [6], or TAGS [7] show good TE properties, but are expensive and toxic, hindering their wider applicability.

Alternative TE materials must be developed for cost-effective, non-toxic, and scalable energy production. A promising material, is the Heusler compound Fe₂VAl [8]. Fe₂VAl is highly durable [9] and contains earth-abundant elements. It is a semimetal with a sharp pseudogap, which is favorable for TE applications [10,11]. Although the power factor is high (>5 mW m⁻¹ K⁻² at 300K), its high thermal conductivity (κ) is limits its TE performances [8]. Doping [10,12–14], off-stoichiometry [15,16], introduction of defects and

exploiting disorder in the structure [17–20] have been explored to enhance phonon scattering and decrease κ .

Another, not as widely studied way of introducing phonon scattering centers is to introduce interfaces, and in particular antiphase boundaries (APB). APBs can be generated inside the L₂₁ Heusler phase by fast quenching from high temperatures, where Fe₂VAl is stable in two variants: partly disordered B2 and fully disordered A2, as described by Maier et al. [19]. A method for achieving the necessary high cooling rates is melt spinning. The melt is dropped onto a cooled, rotating metallic wheel and leading to rapidly quenched flakes. A schematic of two antiphase domains (APD) in the L₂₁ phase separated by an APB is visualized in the supplementary figure S1a. The APDs can be converted into each other by a {100}_{B2} translation, which exists in the disordered B2 structure but is missing in the ordered L₂₁ structure [21]. Another possible interface (Fig. S1b) is a coherent order-disorder boundary. The ordered L₂₁ phase and disordered B2 or A2 phase are coexisting without a change in the crystallographic orientation.

Here, we show evidence for segregation and precipitation in the bulk and at interfaces in melt spun Fe₂VAl. We cannot differentiate specifically between different coherent interfaces, and for readability, boundaries observed and discussed herein will be referred to as APBs. Using scanning electron microscopy (SEM), atom probe tomography (APT) and field ion microscopy (FIM), we report on vanadium carbo-nitrides at APBs. These could act as phonon

* Corresponding authors.

E-mail addresses: alleno@icmpe.cnrs.fr (E. Alleno), b.gault@mpie.de (B. Gault).

¹ present address: Institute of Nanotechnology, Karlsruhe institut für technology, Hermann-von-Helmholtzplatz 1, 76344, Eggenstein-Leopoldshafen, Germany

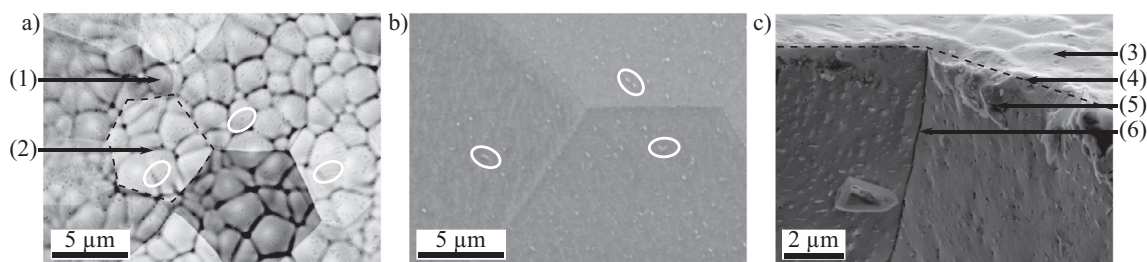


Fig. 1. SEM images of melt spun Fe₂VAl. The white circles indicate exemplary positions where platelet-shaped precipitates are observed. a) BSE image of an unpolished melt spun flake, (1) small surface grains, (2) regular grains. b) SE image of the polished sample, showing the regular grains and precipitates within the flake. c) cross section view along the edge of an unpolished sample, (3) surface grains observed from the surface of the flake, (4) edge of the sample, indicated by the dashed line, (5) surface grains layer observed from the cross section, (6) grain boundary of lower lying regular grains.

scattering centers and hence open opportunities for further microstructural adjustments for lowering the thermal conductivity.

Stoichiometric Fe₂VAl was synthesized by melt spinning. The pure elements Fe (Strem Chemicals, 99.95%), V (Chempur, 99.9%), and Al (Alfa Aesar, 99.9965%) were melted together and subsequently ejected at 1490°C onto a water-cooled, rotating CuCoBe wheel spinning at 24.5 m/s, ensuring a fast quenching rate. This process leads to approximately 20 μm thick flakes. Inductively Coupled Plasma Optical Emission Spectrometry determined the average chemical composition to be Fe_{50.54}V_{24.81}Al_{24.65} (at.%). X-ray diffraction (XRD) indicates the presents of the L2₁ ordered phase (Fig. S2). However, the co-existence of B2 and A2 phase cannot be excluded from the XRD pattern.

Microscale analyses of the microstructure were performed using scanning electron microscopy (SEM) and energy-dispersive X-ray spectroscopy (EDX) using a Zeiss 1540 XB SEM. The samples were analyzed as-cast without any polishing, and after hand grinding to observe the microstructure on the surface and inside the sample. The sample was initially prepared using SiC papers and final polishing was done using a colloidal silica suspension (0.25 μm) in a vibrating polishing machine (Buehler Vibromet 2).

Near-atomic scale investigations were performed using FIM and APT. Needle-shaped specimens for APT and FIM were prepared using a dual-beam focused-ion-beam (FIB) instrument (FEI Helios Nanolab600i) with a Ga ion source or an FEI Helios Plasma-FIB with a Xe-plasma ion source by an in-situ lift-out method and a subsequent sharpening process [22]. For correlative FIM/APT analysis, a LEAPTM 5000 XS (Cameca Instruments) was used. APT was conducted in voltage pulsing mode using a pulse repetition rate of 125 kHz and a pulse fraction of 15%. For FIM, Ne was used as an imaging gas to image the sample surface at 50K. The Ne gas pressure while imaging was kept at 1•10⁻⁷ mbar and, when possible, images were acquired at the best imaging voltage. APT measurements were also performed on a LEAPTM 5000 XR (Cameca Instruments) in laser-pulsing mode. The laser power was set to 25 pJ and the repetition rate was 250 kHz. For both APT measurements, the base temperature of the specimen was kept at 60 K and a target detection rate was set to 0.5%. The IVAS 3.8.4 software and MATLAB 2017a were used for data reconstruction and analysis.

Fig. 1 presents backscattered electron (BSE) and secondary electron (SE) micrographs of the unpolished and mechanically polished samples as well as a cross sectional image. Parallel to the surface (Fig. 1a), the BSE image shows two layers of grains, which we will call surface grains and regular grains in the following. On the surface of the flake, grains with a mean size of (1.7 ± 0.1) μm (Fig. 1a, (1)) are observed. The grain size of grains within the flake is (5.5 ± 0.4) μm (Fig. 1a, (2)). The SEM image used for the analysis of the mean grain sizes is shown in the supplemental data Fig. S3. Both layers are visible due to the interaction volume of the electron beam and the material, which is in the order of 1 μm for

an acceleration voltage of 15 kV and therefore can penetrate the flake deeper than the mean thickness of the surface grains. Fig. 1b shows a polished surface, where only the regular grains are observed as the surface layer is polished away. The small surface grains can also be seen in Fig. 1c on the edge of the flake (4), where they are observed from the surface (3) and the cross section (5). EDX was used to analyze grain-to-grain compositional variations. No significant changes could be observed, as presented in Fig. S4.

All SEM images show platelet-like precipitates at the grain boundaries and inside the grains. These precipitates are highlighted by white circles. The precipitates within one grain are oriented either parallel or perpendicular to each other (Fig. 1a, c), but their orientation differs between grains (Fig. 1a). This indicates that the orientation of the precipitates is dependent on the crystallographic orientation of the grains. The 90° angle between precipitates within one grain (Fig. 1c) could indicate that the precipitates are on {100} planes. The average size of these precipitates is 120 × 40 nm² and they are separated by a mean distance of (140 ± 40) nm.

APT and FIM are used to confirm the presence of ordered phases and antiphase boundaries while analyzing the elemental distribution at the near-atomic scale. A field-ion micrograph is displayed in Fig. 2a. It shows two ordered domains separated by a bright-imaging feature and indicated by black arrows. The ordering of the right domain is revealed for instance by the relative contrast at the (111)-pole [23]. It consists of rings with alternating intensities, indicating planes with different atomic occupancies. This is true for the L2₁ phase, where a {111} plane, occupied by Fe atoms, sandwiches alternating Al and V planes, as visualized in Fig. 2b. The B2 phase consists of {111} planes occupied by Fe, followed by planes with a mixed occupancy of Al and V. Thus, only the A2 phase can be excluded from this FIM micrograph. The rings formed by {110} planes do not show any alternating intensity, as the planes are occupied with Fe, V, and Al, even in L2₁ ordering. The other domain on the left part of the micrograph shows the (100) pole. Ordering on that pole cannot be directly observed because of the small interplanar distance and associated limited resolution. The two domains appear coherent, as evidenced by the pattern continuity at the (101) pole across the interface. The contrast of the interface indicates that it is decorated by high-evaporation field elements. This coherent boundary is likely a typical APB (Fig. S1a) or an interface between an ordered and a disorder region (Fig. S1b).

Correlative APT and FIM is shown in Fig. 3: FIM was performed before and after APT as indicated by the light blue and dark blue circles, respectively. During the APT measurement, approximately 56.7 million ions were detected and the analysis was stopped when a strong planar segregation appeared. The specimen fractured before FIM could be performed in the best imaging conditions, yet poles observed in both FIM micrographs are at

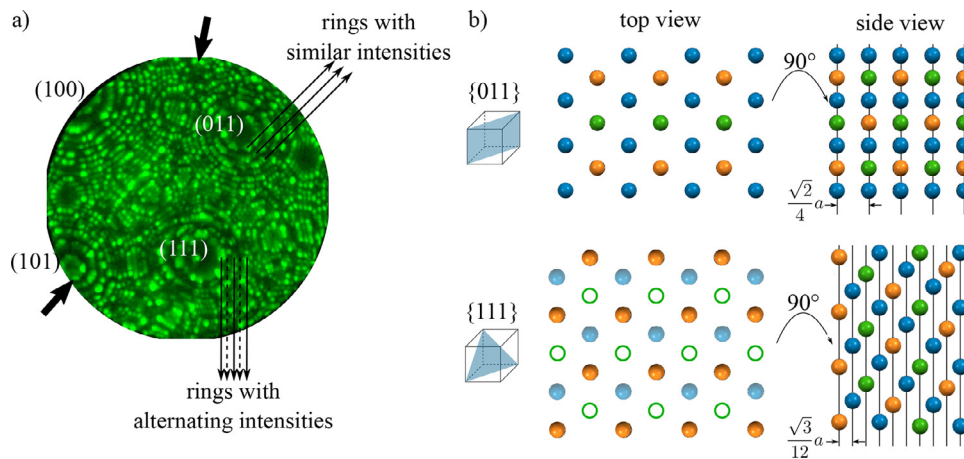


Fig. 2. a) FIM micrograph showing two domains separated by a coherent boundary. The boundary is marked by the arrows. The (111) pole shows rings with alternating intensities due to an ordering of the {111} lattice planes. b) Visualization of the {011} and {111} planes of the L21 phase. Fe, V, and Al are displayed as blue, green, and orange spheres, respectively. The {011} plane shows a mixed coverage on parallel planes. Along the {111} planes, a plane occupied by Al is followed by a Fe-plane (half-transparent spheres), which is followed by a V-plane (green circles). The side view is rotated by 90° with regards to the top view, showing the crystallographic sequence of the corresponding planes, which are indicated by the black lines.

the same positions, and can be indexed according to their Miller indices (Fig. 3a). The (111) pole, exhibiting a 3-fold symmetry, is observed near the center. The planar feature seen in APT appears as a brightly-imaging feature across the field-of-view in the second FIM image. The poles on either side of this feature seem to be at the same position, which indicates no change in the crystallographic orientation across this interface, which reinforces the likelihood that this is an APB. The crystallographic orientation of the APB can be observed in the AP reconstruction. A desorption map before and at the APB is shown in Fig. 3b. The different poles can be indexed similarly to the FIM micrographs. Within the vicinity of the poles, the crystallographic planes can be indexed [24], which allows us to determine that this APB lies on the {100} plane.

The AP reconstruction of a small region across the boundary shows {011} planes on either side of the boundary (Fig. 3d). The angle between the APB, visualized by the iso-composition interface, and the planes is approximately 45°, which supports the {100}-orientation of the APB. The spatial distribution map, visualizing the distance of the planes on either side of the boundary is given in the supplemental figure S5. This further indicates that same sets of planes are imaged on either side of the APB as their separation is similar.

As shown in Fig. S1 an APB can exist without any change in the chemical composition. However, similar to grain boundaries, an energetically driving force for segregation exists at an APB and was analyzed theoretically for Fe₃Al [21]. The APB appears to be segregated to a point where they can trigger precipitation of VC_xN_y. Here, we observe coherent precipitation of V, C, and N in the form of VC_xN_y, as evidenced by the iso-composition interface in the AP reconstruction (Fig. 3c). The iso-composition interface marks regions with a concentration of C, N, VC, and VN-ions of at least 3 at.%. Within the matrix, a smaller spherical VN_y precipitate is found, which is also shown by the iso-composition interface.

A closer look at an APB in another dataset is shown in Fig. 4. A set of iso-composition surfaces, with the same threshold as in Fig. 3, highlights two larger and a smaller platelet-shape precipitate (Fig. 4c). The density map on either side of the APB shows a continuity of the position of the (100) pole (Fig. 4a). Within a region-of-interest close to the pole, the planes and the APB appear parallel, as shown in Fig. 4b, confirming that the APB lies on the {100} plane. A composition profile was calculated along a 20 nm-diameter cylindrical region-of-interest with a step size of 0.3 nm (Fig. 4d). On either side of the APB, the composition is near-stoichiometric. In the vicinity of the APB, highlighted by the gray box, an enrichment of V, C, and N is observed, and its composi-

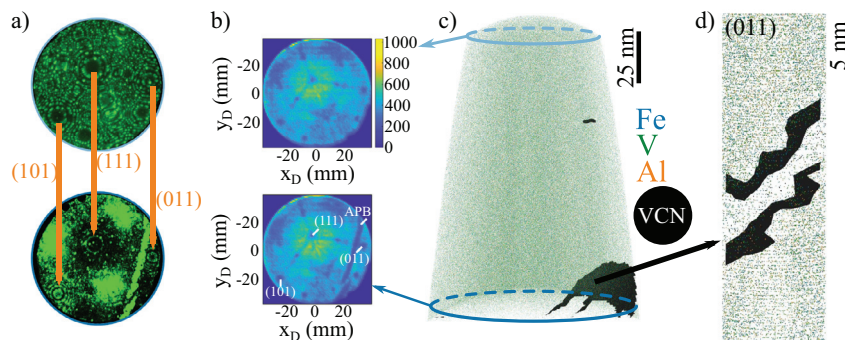


Fig. 3. Correlative APT and FIM study. a) FIM micrographs, conducted before and after the APT run, as indicated by the blue circles. The orange arrows mark the poles visible in both FIM images, which show no change in the crystallographic orientation on either side of the precipitates indicating an APB. b) AP desorption maps, showing the same poles as the FIM micrographs. c) AP reconstruction showing the elemental distribution of Fe, V, and Al ions and an iso-composition interface with 3 at.% VC_xN_y as labeled next to the reconstructed data. The iso-composition interface shows a platelet-shaped VC_xN_y precipitate at the APB and a smaller VN_y precipitate within the matrix. d) AP reconstruction of (011) planes around the APB. On either side of the APB, parallel planes are observed.

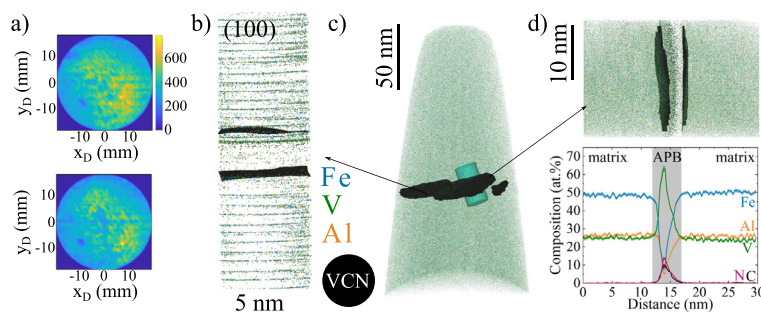


Fig. 4. AP reconstruction of a second specimen. a) Desorption map showing the (100) pole before and after the APB. b) close-up within the reconstruction on the (100) planes near the APB. On either side of the APB, the parallel planes are observed. c) fully reconstructed volume, showing the elemental distribution of Fe, V, and Al ions and an iso-composition interface with 3 at.% VCxNy as labeled next to the reconstructed data. A platelet-shaped precipitate is observed at an APB. d) composition profile calculated in a cylindrical region of interest with a diameter of 20 nm and a step size of 0.3 nm. An enrichment of V, N, C is found at the APB.

tion is $V_{63.2 \pm 1.7}N_{13.5 \pm 1.1}C_{9.6 \pm 0.9}Fe_{8.2 \pm 0.8}Al_{5.3 \pm 0.7}$ (at.%). These suggest precipitates with a stoichiometry close to $(V,Fe,Al)_3(C,N)$. Along the APB, outside of the precipitate, the concentration of C and N is low with (0.10 ± 0.02) at.% and (0.08 ± 0.01) at.%, respectively. The composition of the precipitates in both APT measurements is similar (Fig. S6).

Carbon and nitrogen were not intentionally introduced. However, both are common impurities in commercial vanadium and iron pellets and may originate from the atmosphere during processing. Vanadium has high affinity with carbon and nitrogen and, during the melt spinning process, it can form carbides at 800–1000 °C and nitrides above 800 °C [25]. The tendency for segregation can be related to the relatively high APB energy of Fe_2VAl is 0.27 ± 0.04 J/m² for an $(\frac{1}{2})1\bar{1}\bar{1}(01\bar{1})$ APB [26], compared to e.g. 0.08 ± 0.03 J/m² for Fe_3Al [27]. The high APB energy is a driving force for segregation, which can reduce its energy [28,29]. It was shown, that Cr segregation to APBs in Fe_3Al can either reduce or enhance the APB energy, depending on the position of the impurities within the matrix [27]. The locally higher composition in V, C, N can help trigger further precipitation [30]. For Fe_3Al , Koizumi et al. [31] described a stabilization of APBs due to segregation of solute atoms and vacancies.

The high affinity of vanadium to form carbides and nitrides offers opportunities to intentionally add C and N and trigger additional precipitation. Carbides and nitrides might further increase phonon scattering and have interesting effects on the transport properties of the material. This combination of nanoprecipitates and APBs should reduce the thermal conductivity. To have a significant influence, the mean phonon free path needs to be longer than the mean distance of the precipitates. For Fe_2VAl at room temperature, the mean free phonon path was estimated to be 2.4 μm. The mean distance of ~140 nm between the platelet-shaped precipitates, observed in the microscale SEM images, is smaller than the phonon mean free path. Additionally, the platelet-shaped precipitates are located at APBs, which give rise to another phonon scattering center. The experimental investigation and calculation of the thermoelectric properties of Fe_2VAl , considering the APB and VCxNy precipitates, are beyond the scope of this paper. Nonetheless, they will be part of future work.

To summarize, we investigated the microstructure of Fe_2VAl , synthesized via melt spinning. We performed microstructural observations using electron microscopy and investigated the composition of APBs and precipitates at the near-atomic level using atom probe tomography. This approach allows us to gain information on different hierarchical length scales. SEM observations were used to determine the statistical distribution of precipitates and their size on the microscale. Platelet-shaped precipitates are found, separated on average by (140 ± 40) nm. APT reveals the chemistry of the platelet-shaped precipitates to be VCxNy. These precipitates

appear at APBs oriented along the {100} direction, as indicated by APT and FIM measurements. APBs are stabilized in the L2₁ phase due to the fast quenching from the disordered B2 and A2 phase, in which Fe_2VAl is stable at temperatures higher than 1080 °C and 1190 °C, respectively [19]. The APBs and corresponding precipitates may act as phonon scattering centers and lower the thermal conductivity, leading to an improvement of the thermoelectric properties.

Declaration of Competing Interests

The authors declare that they have no known competing financial interests or personal relationships that could have appeared to influence the work reported in this paper.

Acknowledgements

L. G. gratefully acknowledges IMPRS-SurMat and Studienstiftung des deutschen Volkes for funding. U. Tezins and A. Sturm are acknowledged for their technical support at the FIB/APT facilities at MPIE. Benjamin Breitbach is acknowledged for providing XRD data. Partial funding of this work by the "Agence Nationale pour la Recherche" through the contract "LoCoThermH" (ANR-18-CE05-0013-01) is acknowledged by A. D. R. and E. A. S.M. gratefully acknowledges support from Prof. Wuttig and the Deutsche Forschungsgemeinschaft (DFG) through the SFB 917 "Nanoswitches".

Supplementary materials

Supplementary material associated with this article can be found, in the online version, at doi:[10.1016/j.scriptamat.2020.04.037](https://doi.org/10.1016/j.scriptamat.2020.04.037).

References

- [1] G.J. Snyder, E.S. Toberer, *Nat. Mater* 7 (2008) 105–114.
- [2] L. Yang, Z.G. Chen, M.S. Dargusch, J. Zou, *Adv. Energy Mater* 8 (2018) 1–28.
- [3] J. Yang, T. Caillat, *MRS Bull* 31 (2006) 224–229.
- [4] C.S.R. Matthes, D.F. Woerner, T. Caillat, S. Pinkowski, *IEEE Aerosp. Conf. Proc* (2019) (2019-March) 1–9.
- [5] H. Mamur, M.R.A. Bhuiyan, F. Korkmaz, M. Nil, *Renew. Sustain. Energy Rev* 82 (2018) 4159–4169.
- [6] T. Thonhauser, J. Scheidemantel, O. Sofo, V. Badding, D. Mahan, *Phys. Rev. B - Condens. Matter Mater. Phys* 68 (2003) 1–8.
- [7] E.M. Levin, S.L. Bud'ko, K. Schmidt-Rohr, *Adv. Funct. Mater* 22 (2012) 2766–2774.
- [8] E. Alleno, *Metals (Basel)* 8 (2018) 864.
- [9] M. Mikami, T. Kamiya, K. Kobayashi, *Thin Solid Films* 518 (2010) 2796–2800.
- [10] H. Al-Yamani, B. Hamad, *J. Electron. Mater* 45 (2016) 1101–1114.
- [11] I. Knapp, B. Budinska, D. Milosavljevic, P. Heinrich, S. Khmelevskiy, R. Moser, R. Podloucky, P. Prenninger, E. Bauer, *Phys. Rev.* 96 (2017) 045204 B.
- [12] W. Lu, W. Zhang, L. Chen, *J. Alloys Compd* 484 (2009) 812–815.
- [13] M. Mikami, K. Kobayashi, *J. Alloys Compd* 466 (2008) 530–534.

- [14] K. Renard, A. Mori, Y. Yamada, S. Tanaka, H. Miyazaki, Y. Nishino, *J. Appl. Phys* (2014) 115.
- [15] H. Miyazaki, S. Tanaka, N. Ide, K. Soda, Y. Nishino, *Mater. Res. Express* (2014) 1.
- [16] Y. Nishino, H. Kato, M. Kato, U. Mizutani, *Phys. Rev. B - Condens. Matter Mater. Phys* 63 (2001) 3–6.
- [17] S. Bandaru, A. Katre, J. Carrete, N. Mingo, P. Jund, *Nanoscale Microscale Thermophys, Eng* 21 (2017) 237–246.
- [18] D.I. Bile, P. Ghosez, *Phys. Rev. B - Condens. Matter Mater. Phys* 83 (2011) 1–6.
- [19] S. Maier, S. Denis, S. Adam, J.C. Crivello, J.M. Joubert, E. Alleno, *Acta Mater.* 121 (2016) 126–136.
- [20] C. Venkatesh, V. Srinivas, V.V. Rao, S.K. Srivastava, P. Sudheer Babu, *J. Alloys Compd* 577 (2013) 417–425.
- [21] H. Wondratschek, W. Jeitschko, *Acta Crystallogr* 32 (1976) 664–666.
- [22] K. Thompson, D. Lawrence, D.J. Larson, J.D. Olson, T.F. Kelly, B. Gorman, *Ultra-microscopy* 107 (2007) 131–139.
- [23] X.J. Ge, N.X. Chen, W.Q. Zhang, F.W. Zhu, *J. Appl. Phys* 85 (1999) 3488–3493.
- [24] B. Gault, M.P. Moody, J.M. Cairney, S.P. Ringer, *Atom Probe Microscopy*, Springer Series in Material Science, New York, 2012.
- [25] G. Bauer, V. Güther, H. Hess, A. Otto, O. Roidl, H. Roller, S. Sattelberger, S. Köther-Becker, T. Beyer, *Ullmann's Encycl. Ind. Chem* (2016).
- [26] P.A. Ferreirós, P.R. Alonso, G.H. Rubiolo, *Mater. Sci. Eng. A* 684 (2017) 394–405.
- [27] M. Friák, M. Všíanská, M. Šob, *Materials (Basel)* 12 (2019) 1–15.
- [28] S.K. Makineni, M. Lenz, S. Neumeier, E. Spiecker, D. Raabe, B. Gault, *Scr. Mater.* 157 (2018) 62–66.
- [29] R. Kikuchi, J.W. Cahn, *Acta Metall* 27 (1979) 1337–1353.
- [30] P.R. Swann, *Philos. Mag* 14 (1966) 461–471.
- [31] Y. Koizumi, S.M. Allen, Y. Minamino, *Acta Mater* 57 (2009) 3039–3051.